Identification of the hydrogen-saturated self-interstitials in silicon and germanium

M. Budde and B. Bech Nielsen
Institute of Physics and Astronomy, University of Aarhus, DK-8000 Aarhus, Denmark

P. Leary, J. Goss, and R. Jones
Department of Physics, University of Exeter, Exeter, EX4 4QL, United Kingdom

P. R. Briddon
Department of Physics, University of Newcastle upon Tyne, Newcastle upon Tyne, NE1 7RU, United Kingdom

S. Öberg
Department of Mathematics, University of Luleå, Luleå, Sweden

S. J. Breuer
Edinburgh Parallel Computing Centre, University of Edinburgh, Edinburgh, EH9 3JZ, United Kingdom
(Received 16 July 1997)

Silicon and germanium single crystals are implanted with protons. The infrared-absorption spectra of the samples contain sharp absorption lines due to the excitation of hydrogen-related local vibrational modes. The lines at 743.1, 748.0, 1986.5, and 1989.4 cm^{-1} in silicon and at 700.3, 705.5, 1881.8, and 1883.5 cm^{-1} in germanium originate from the same defect in the two materials. Measurements on samples coimplanted with protons and deuterons show that the defect contains two equivalent hydrogen atoms. Uniaxial stress measurements are carried out and a detailed analysis of the results is presented. It is shown that the defect has monoclinic-II symmetry, and the orientations of the Si-H and Ge-H bonds of the defect are determined. *Ab initio* local-density-functional theory is used to calculate the structure and local vibrational modes of the self-interstitial binding one and two hydrogen atoms in silicon and germanium together with the structure of the self-interstitial itself. The observed properties of the defect are in excellent agreement with those calculated for the self-interstitial binding two hydrogen atoms. [S0163-1829(98)06104-9]

I. INTRODUCTION

The vacancy and the self-interstitial are the fundamental intrinsic point defects in crystalline silicon. Both defects can be produced by irradiation with electrons, neutrons, or ions. The vacancy in silicon has been studied in great detail,[1] and it is one of the best-characterized point defects in any crystalline material. In contrast, the self-interstitial in silicon has never been observed directly. Instead, interstitial impurities such as boron, carbon, aluminum, or gallium are observed after irradiation.[1] It is believed that the self-interstitials are mobile during the irradiation process and that interstitial impurities are created by a kick-out mechanism.[1] Thus, our present knowledge about the self-interstitial is based on studies of the products of such reactions and on theoretical calculations.[2–6]

A major objective in defect studies is to determine the microstructure of the defects, which is essential for a detailed understanding of their properties. Theoretical calculations[2–6] suggest that the minimum-energy configuration of the self-interstitial in the neutral charge state is a $\langle 110 \rangle$ split, in which two silicon atoms share a lattice site as shown in Fig. 1(a). Unfortunately, it may be impossible to check the theoretical predictions experimentally due to the high mobility and reactivity of the self-interstitial. Therefore, the best way to obtain microstructural information may be to study reaction products that are stable and closely resemble the self-interstitial. Two obvious candidates of such products are the self-interstitial binding one or two hydrogen atoms. These complexes are expected to exist, since hydrogen interacts strongly with dangling bonds.[7,8] The addition of hydrogen may immobilize the self-interstitial and, thus, the complexes may be stable even at room temperature. The length of the molecular Si-H bond ($\sim$1.48 Å) is considerably shorter than that of the Si-Si bond ($\sim$2.35 Å), which suggests that Si-H bonds may be formed in the open parts of the lattice without introduction of substantial strain. Consequently, the rearrangement of the self-interstitial introduced by trapping of

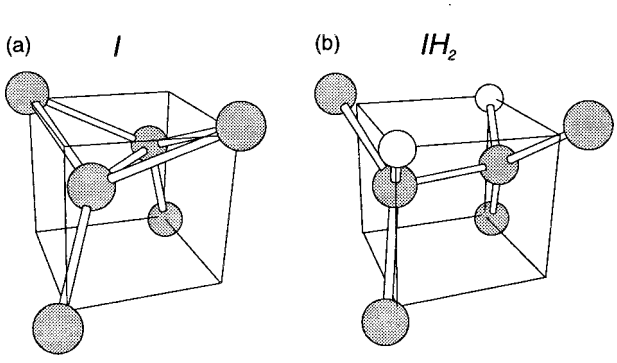

FIG. 1. Calculated structure of (a) the self-interstitial I and (b) the hydrogen-saturated self-interstitial IH_2 in silicon (Ref. 6). The shaded spheres are silicon, whereas the white spheres are hydrogen.

hydrogen could be moderate. Theoretical calculations confirm that the silicon self-interstitial can trap up to two hydrogen atoms.[9,10,6] The minimum-energy configurations of the self-interstitial I and the hydrogen-saturated self-interstitial IH_2 found by Van de Walle and Neugebauer[6] are shown in Fig. 1. The positions of the two central silicon atoms change by only 0.66 Å (see Ref. 6) when two hydrogen atoms are introduced. Hence, an experimental determination of the microstructure of IH_2 may provide a direct check of the credibility of the theoretical structures of IH_2 and I.

Infrared-absorption spectroscopy is an excellent tool for investigating the local vibrational modes of hydrogen-related defects in silicon[11–13] and germanium.[14] The local-mode frequencies give information about the chemical bonding of the hydrogen, and the number of hydrogen atoms involved in the defect can often be determined from measurements on samples co-doped with hydrogen and deuterium.[13] In addition, the symmetry of the defect may be obtained from the splittings of the absorption lines induced by uniaxial stress.[12,13]

In proton-implanted silicon, Si:H, a series of absorption lines that correspond to Si-H stretch modes are observed in the frequency range 1800–2250 cm^{-1} together with lines of Si-H bend modes in the range 700–850 cm^{-1}. Of particular interest for this work is the line observed at 1980 cm^{-1} at room temperature.[11] This line was also observed in hydrogen-doped silicon irradiated with electrons,[15] neutrons,[16] or γ rays,[17] and it was found to split into a doublet of lines at 1987 and 1989 cm^{-1} when the sample temperature was reduced to 10 K.[15] The two lines displayed the same production and annealing behaviors, which indicates that they originate from the same defect.[15,16] These observations led Xie, Qi, and Chen [Ref. 16] to assign the 1987- and 1989-cm^{-1} lines to the monovacancy containing two hydrogen atoms VH_2. However, this assignment disagrees with recent work,[8] in which absorption lines at 2121 and 2144 cm^{-1} were identified as the Si-H stretch modes of VH_2. Thus, the origin of the 1987- and 1989-cm^{-1} lines remains unclear.

In this paper, four Si-H modes observed at 743.1, 748.0, 1986.5, and 1989.4 cm^{-1} in Si:H and four similar Ge-H modes observed at 700.3, 705.5, 1881.8, and 1883.5 cm^{-1} in Ge:H are studied in detail. Annealing studies show that the four modes in each material originate from the same defect, which by isotope substitution is found to contain two equivalent hydrogen atoms. Uniaxial stress measurements show that the defect has monoclinic-II symmetry, and the orientations of the two Si-H and Ge-H bonds are determined. Based on the experimental evidence, the four Si-H and Ge-H modes are assigned to IH_2 in silicon and germanium. The experimental results are compared with the results of *ab initio* calculations on IH_2 in silicon and germanium. All calculated properties are in close agreement with those observed. This provides strong support to our assignments.

II. EXPERIMENTAL DETAILS

A. Sample preparation

Samples were cut from high-resistivity, float-zone single crystals of silicon and germanium, and were mechanically and electrically polished. The samples for isochronal annealing and isotope substitution studies had dimensions of $10\times10\times2$ mm^3, whereas the uniaxial stress measurements were carried out on samples with dimensions $10\times2\times2$ mm^3 with the 2×2-mm^2 surfaces cut perpendicular to [100], [111], or [110] directions. The samples were mounted on a 4-mm-thick copper block, which was in good thermal contact with a closed-cycle helium cryocooler. This setup allowed the samples to be cooled to ~30 K during the implantation. Each sample was implanted with protons and/or deuterons at 50–100 equidistant energies in the range 680–2500 keV for protons and 840–3000 keV for deuterons. The dose at each energy was adjusted to result in a uniform hydrogen or deuterium concentration of 0.02 or 0.05 at. % in the range 8–60 μm below the surface of the silicon samples, and a concentration of 0.05 at. % from 11 to 44 μm below the surface of the germanium samples. Some samples were coimplanted with protons and deuterons in equal concentrations and overlapping profiles. In order to obtain a uniform lateral distribution of implants, the ion beam was swept in two perpendicular directions over an area twice as large as the 6×12 mm^2 spot defined by the beam slits. The beam current was measured with a Faraday cup located ~1 m behind the slits and ~2 m in front of the sample. At each energy, the current averaged over a period of 1 min. was measured and used to estimate the implantation time needed to yield the planned dose. The variations in the current were less than 10%, which gives a measure of the uncertainty of the implanted dose. After implantation, the samples were stored at room temperature.

B. Infrared absorption measurements

The absorption of infrared light penetrating the samples perpendicular to the implanted surface was measured with a Nicolet, System 800, Fourier-transform spectrometer, equipped with a glowbar source, a Ge on KBr beamsplitter and an MCT (mercury cadmium telluride) detector. With this configuration, reliable absorption measurements can be made in the frequency range 600–6000 cm^{-1}. The annealing and isotope substitution studies were performed using either a closed-cycle helium cryostat or a flow-cryostat both with CsI windows. The uniaxial stress measurements were carried out with the flow cryostat equipped with two sets of windows made of CsI and BaF_2. Due to the strong absorption of BaF_2 below ~725 cm^{-1}, the spectral range in these experiments was reduced accordingly. The absorption measurements for the annealing and isotope substitution studies were performed at 77 K with a resolution of 0.6 cm^{-1} in the case of silicon, and at 10 K with a resolution of 0.5 cm^{-1} for germanium. The uniaxial stress studies were carried out with a home-built stress rig mounted in the flow cryostat. The stress was supplied by a pneumatic cylinder and transferred via a push rod to the sample. A polarizer was placed between the sample and the detector, so that the absorption of infrared light polarized parallel and perpendicular to the applied force could be measured separately. The uniaxial stress measurements on silicon were performed at 4.2 and 77 K with a resolution of 0.5 cm^{-1}, and on germanium at 77 K with a resolution of 0.8 cm^{-1}.

TABLE I. The first-order stress pattern of a center with monoclinic-II symmetry (Ref. 18). The dipole moment is parallel to the C_2 axis for the $|A\rangle \rightarrow |A\rangle$ transition. For the $|A\rangle \rightarrow |B\rangle$ transition, the dipole moment is in the plane perpendicular to the C_2 axis with the angle φ to a $\langle 100 \rangle$ direction in this plane.

		Transitions			
		$\|A\rangle \rightarrow \|A\rangle$		$\|A\rangle \rightarrow \|B\rangle$	
	Frequency shift	$I_{\parallel}$	$I_{\perp}$	$I_{\parallel}$	$I_{\perp}$
F//[100]	$\mathcal{A}_1\sigma$	4	0	0	2
	$\mathcal{A}_2\sigma$	0	2	$4\sin^2\varphi$	$2\cos^2\varphi$
	$\mathcal{A}_3\sigma$	0	2	$4\cos^2\varphi$	$2\sin^2\varphi$
	Frequency shift	$I_{\parallel}$	$I_{\perp}$	$I_{\parallel}$	$I_{\perp}$
F//[111]	$\frac{1}{3}(\mathcal{A}_1+\mathcal{A}_2+\mathcal{A}_3+2\mathcal{A}_4)\sigma$	2	2	$2+2\sin 2\varphi$	$2-\sin 2\varphi$
	$\frac{1}{3}(\mathcal{A}_1+\mathcal{A}_2+\mathcal{A}_3-2\mathcal{A}_4)\sigma$	2	2	$2-2\sin 2\varphi$	$2+\sin 2\varphi$
	Frequency shift	$I_{[110]}$	$I_{[001]}$	$I_{[1\bar{1}0]}$	$I_{[110]}$	$I_{[001]}$	$I_{[1\bar{1}0]}$
F//[110]	$\frac{1}{2}(\mathcal{A}_2+\mathcal{A}_3+2\mathcal{A}_4)\sigma$	0	2	0	$1+\sin 2\varphi$	0	$1-\sin 2\varphi$
	$\frac{1}{2}(\mathcal{A}_2+\mathcal{A}_3-2\mathcal{A}_4)\sigma$	0	2	0	$1-\sin 2\varphi$	0	$1+\sin 2\varphi$
	$\frac{1}{2}(\mathcal{A}_1+\mathcal{A}_2)\sigma$	2	0	2	$2\sin^2\varphi$	$4\cos^2\varphi$	$2\sin^2\varphi$
	$\frac{1}{2}(\mathcal{A}_1+\mathcal{A}_3)\sigma$	2	0	2	$2\cos^2\varphi$	$4\sin^2\varphi$	$2\cos^2\varphi$

III. STRESS PATTERN OF A MONOCLINIC-II DEFECT

When uniaxial stress is applied to a crystal, the quantum states of the system are perturbed. Since the energies of two different states normally change differently, the frequency that corresponds to an optical transition between the two states quite generally shifts as a function of the magnitude of the stress. For a noncubic defect in silicon or germanium, a number of different orientations of the defect exist. In the absence of stress all orientations are equivalent and, hence, for a given transition a single absorption line is observed. In the presence of uniaxial stress, the frequency shift of the transition depends on the orientation of the defect with respect to the stress direction. Consequently, the uniaxial stress will cause the single absorption line to shift and split into a specific number of components determined by the symmetry of the defect and the stress direction. In the case of transitions involving degenerate states, additional splittings may occur due to the lifting of this degeneracy by the stress perturbation. In all cases, the stress-induced shifts and splittings can be accounted for by a small number of adjustable parameters.[18,19] Provided that the defects do not reorient and are distributed evenly over the different orientations, the relative intensities of the stress-split components depend only on the orientation of the optically active dipoles and the polarization of the light.[18,19] Thus, for a specific direction $[hkl]$ of the uniaxial stress and a specific polarization $[h'k'l']$ of the light,[20] the stress-induced frequency shifts and splittings together with the relative intensities of the stress-split components define a pattern, which depend on the symmetry of the defect and on the orientation of the optically active dipole. In the following, we shall refer to this as *the stress-pattern for* $[hkl]$ *stress and* $[h'k'l']$ *polarization* of the transition. The collection of stress patterns for [100], [111], and [110] stresses is henceforth denoted *the stress pattern* of the transition.[21]

In this work, monoclinic-II symmetry is of particular interest. A defect in a diamond-type lattice belonging to this symmetry class has a C_2 point group, which apart from the identity operation E contains only a C_2 element along an $\langle 100 \rangle$ axis. Kaplyanskii[18] derived the stress pattern for a transition of a monoclinic-II defect under the assumption that the stress-induced perturbation is linear in the components σ_{ij} of the stress tensor (see Table I). The electric dipole moment involved in an optical transition is either parallel or perpendicular to the C_2 axis. Kaplyanskii treated the former case in detail,[18] but in the latter case he calculated the relative intensities for a *circular oscillator* in which two perpendicular dipoles are equally active. Circular oscillators do not occur in practice and, therefore, we have generalized Kaplyanskii's calculation of the relative intensities to comply with all orientations of a single dipole in the plane perpendicular to the C_2 axis. The results are given in Table I.

IV. EXPERIMENTAL RESULTS

A. Infrared absorption spectra

The implantation of protons into silicon gives rise to about 20 sharp absorption lines in the range $1800-2250\ \mathrm{cm}^{-1}$, as shown in Fig. 2. When deuterons are implanted, the lines are shifted in frequency by a factor $\sim 1/\sqrt{2}$, which establishes that the absorption lines reflect the excitations of hydrogen-related local vibrational modes. In agreement with previous assignments,[8,11,13] we ascribe these lines to Si-H stretch modes. In addition, about 10 sharp absorption lines are observed in the range $700-850\ \mathrm{cm}^{-1}$ in Si:H, and we assign these lines to Si-H bend modes. No counterparts of these lines are observed in the deuteron-implanted samples, presumably because their frequencies are below the detection limit with our setup. Of particular interest in this work are the Si-H modes at 743.1, 748.0, 1986.5, and 1989.4 cm^{-1}, which are shown in the insets of Fig. 2. In the Si:D samples, the frequencies of the two similar stretch modes are 1446.1 and 1448.2 cm^{-1}.

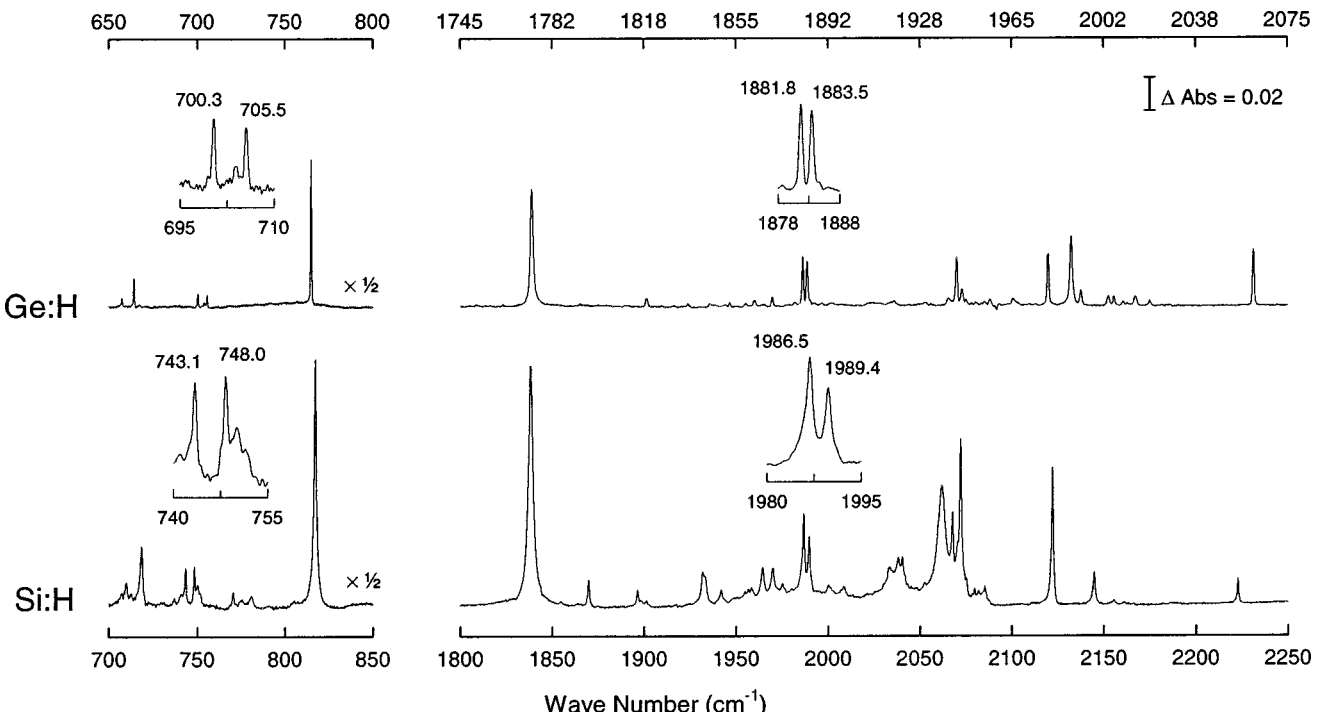

FIG. 2. Absorbance spectra of Si:H (bottom) and Ge:H (top) measured at 8 K after room-temperature annealing. The insets show the lines of particular interest to this work.

In germanium implanted with protons, similar series of absorption lines are observed in the ranges 650–800 cm^{-1} and 1750–2100 cm^{-1} (see Fig. 2). Again, the lines in the high-frequency range are observed to shift in frequency by a factor $\sim 1/\sqrt{2}$ when deuterons are substituted for protons. We assign the lines in the low-frequency range to Ge-H bend modes and those in the high-frequency range to Ge-H stretch modes. The deuterium counterparts of the lines in the low-frequency range are inaccessible with our experimental setup as in the silicon case. Located approximately in the middle of the stretch-mode range of Ge:H is a doublet of lines at 1881.8 and 1883.5 cm^{-1}, which shift down to 1357.6 and 1359.0 cm^{-1} in Ge:D. Another doublet of lines at 700.3 and 705.5 cm^{-1} is observed in the bend-mode range. Within 0.3%, the frequencies of the four Ge-H modes scale with the four Si-H modes specified above. The average frequency ratio between the similar Ge-H and Si-H modes is 0.945, which is within the range of ratios 0.896 to 0.965 obtained for similar modes in germane (GeH_4) and silane (SiH_4).[22] This strongly indicates that the four Si-H and Ge-H modes originate from defects with essentially the same structures in the two materials.

B. Isochronal annealing

An isochronal annealing sequence was performed in which the samples were annealed for 30 min. at each temperature, starting at room temperature and going up to $\sim 500\,^{\circ}C$ in steps of $\sim 20\,^{\circ}C$. The absorbance spectra were measured after each step. The dependencies on the annealing temperature of the four Si-H and Ge-H lines are shown in Figs. 3 and 4. The four lines within each set always appear with the same relative intensities, independent of the annealing temperature and of the implanted dose. This strongly suggests that the four lines originate from the same defect. All other lines in Fig. 2 have different annealing behaviors and do, therefore, not originate from this defect. The set of four lines disappear together at $\sim 225\,^{\circ}C$ in silicon and at $\sim 200\,^{\circ}C$ in germanium. This difference in annealing temperature of the defect in silicon and germanium is comparable to that of the H_2^* defect in the two materials.[13,14] This suggests that the four Si-H and Ge-H modes originate from identical defects in the two materials.

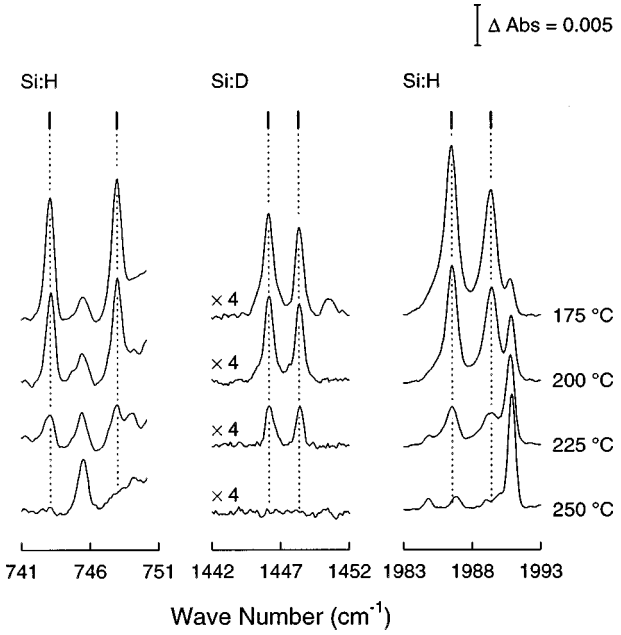

FIG. 3. Isochronal annealing behaviors of the absorption lines at 743.1, 748.0, 1986.5, and 1989.4 cm^{-1} in Si:H and at 1446.1 and 1448.2 cm^{-1} in Si:D.

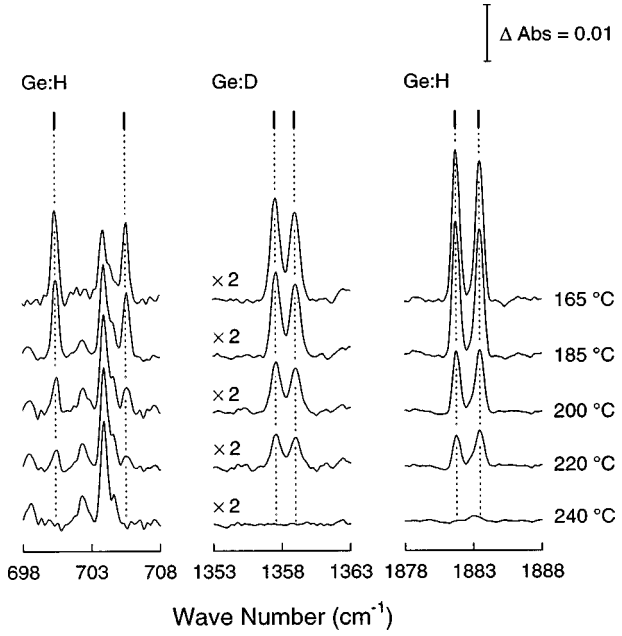

FIG. 4. Isochronal annealing behaviors of the absorption lines at 700.3, 705.5, 1881.8, and 1883.5 cm^{-1} in Ge:H and at 1357.6 and 1359.0 cm^{-1} in Ge:D.

C. Isotope substitution

Absorbance spectra measured on silicon and germanium samples coimplanted with protons and deuterons are shown in the upper part of Figs. 5 and 6. Apart from the lines observed in samples implanted with a single isotope, three additional lines are observed at 745.7, 1447.3, and 1987.8 cm^{-1} in silicon and at ~703, 1358.4, and 1882.8 cm^{-1} in germanium. The additional lines have the same annealing behaviors as the six lines in the single-isotope samples of each material. Therefore, the additional lines are ascribed to isotopically mixed configurations of the same defect. The observation of only two additional stretch-mode lines, of which one involves hydrogen and the other involves deuterium, indicates that the defect contains two equivalent hydrogen atoms. Also the observation of a single additional line in the Si-H bend-mode range is consistent with this. As can be seen from Fig. 6, the additional line at ~703 cm^{-1} in the Ge-H bend-mode range is not resolved convincingly. The intensities of the isotopically mixed lines are generally weak in our germanium samples, and the 703-cm^{-1} line overlaps with a nearby unrelated line.

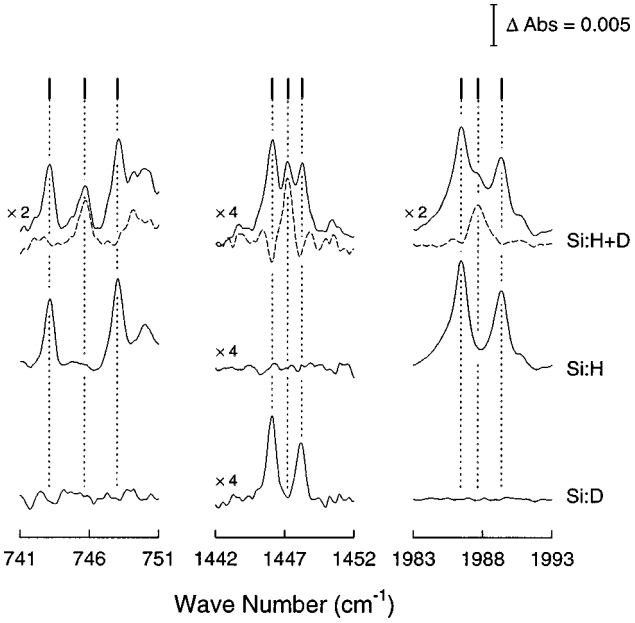

FIG. 5. The result of isotope substitution on the Si-H lines at 743.1, 748.0, 1986.5, and 1989.4 cm^{-1} and the Si-D lines at 1446.1 and 1448.2 cm^{-1}. The dashed line in the upper part of the figure is the Si:H+D spectrum subtracted by the Si:H or Si:D spectrum.

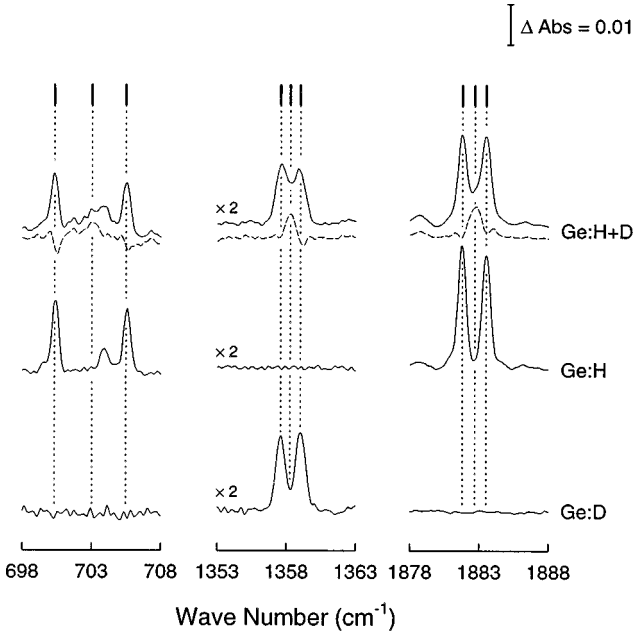

FIG. 6. The result of isotope substitution on the Ge-H lines at 700.3, 705.5, 1881.8, and 1883.5 cm^{-1} and the Ge-D lines at 1357.6 and 1359.0 cm^{-1}. The dashed line in the upper part of the figure is the Ge:H+D spectrum subtracted by the Ge:H or Ge:D spectrum.

D. Uniaxial stress

Both the 1881.8- and 1883.5-cm^{-1} lines in Ge:H split into three components when uniaxial stress is applied along the [100] axis, as shown in Fig. 7. This implies that these ab-

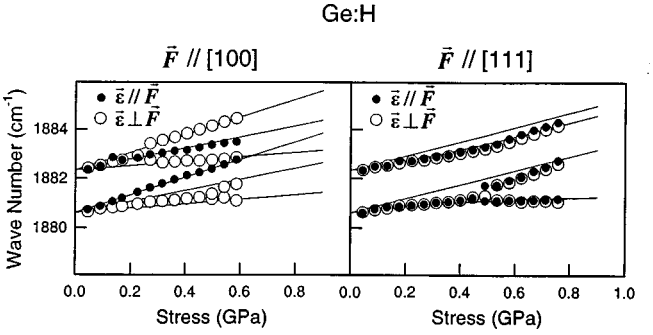

FIG. 7. The stress response of the 1881.8- and 1883.5-cm^{-1} lines in Ge:H for uniaxial stress along [100] and [111] measured at 77 K. The solid (open) symbols correspond to the infrared light polarized parallel (perpendicular) to the applied stress. The solid lines are obtained from the second-order analysis described in Sec. VI with the parameters presented in Table II.

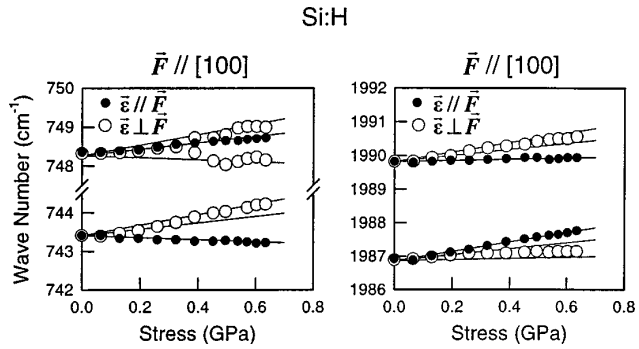

FIG. 8. The stress response of the 743.1-, 748.0-, 1986.5- and 1989.4-cm^{-1} lines in Si:H for [100] stress measured at 4.2 K. The solid (open) symbols correspond to the infrared light polarized parallel (perpendicular) to the applied stress. The solid lines represent the best first-order fit to the data as described in Sec. VI.

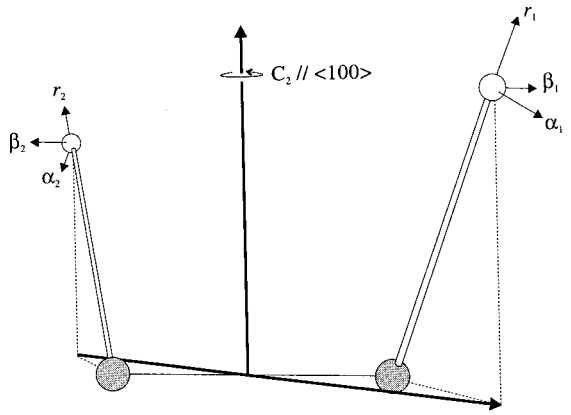

FIG. 9. Illustration of the vibrational modes for a monoclinic-II center containing two equivalent Si-H or Ge-H bonds. The shaded spheres represent silicon or germanium and the white spheres hydrogen. The displacement coordinates r_i, α_i and β_i, $i \in \{1,2\}$, are indicated by arrows.

sorption lines either correspond to one-dimensional modes of a defect with triclinic, monoclinic-II or orthorhombic-II symmetry[18] or to a two-dimensional mode of a center with tetragonal symmetry.[19] The presence of two equivalent Ge-H bonds is only compatible with tetragonal and orthorhombic-II symmetries if the two bonds are aligned with the same ⟨100⟩ axis. This, however, would imply that only one of the two stretch modes should be infrared active, in conflict with the observation of two lines of almost equal intensity. The presence of two equivalent Ge-H bonds also suggests that the point group of the defect possesses at least one symmetry element in addition to the identity operation. Consequently, only monoclinic-II symmetry appears to be in accordance with both the observed splitting under [100] stress and the presence of two equivalent Ge-H bonds. Of course, the stress patterns of the 1881.8- and 1883.5-cm^{-1} lines for [111] and [110] stresses should also be consistent with monoclinic-II symmetry. However, at this point we postpone further discussion of the Ge-H stretch data to Sec. VI, where a detailed analysis is presented. We were unable to study the uniaxial stress responses of the 700.3- and 705.5-cm^{-1} lines as they lie in the frequency range cut off by the BaF_2 windows of the cryostat.

The Si-H lines at 743.1, 748.0, 1986.5, and 1989.4 cm^{-1} are less sensitive to uniaxial stress than the Ge-H lines discussed above. The splitting into three components for [100] stress could not be resolved at 77 K. Therefore, the uniaxial stress response for [100] stress was measured also at liquid-helium temperature where the absorption lines are narrower. The results are shown in Fig. 8. It is evident that the 748-cm^{-1} line splits into three components, indicating the monoclinic-II symmetry also in silicon. For the 743.1-, 1986.5-, and 1989.4-cm^{-1} lines only two components could be resolved. Further discussion of the Si:H data is also postponed to Sec. VI.

V. THE STRESS PATTERN OF IH_2

In this section, the uniaxial stress pattern is derived for the local vibrational modes of a monoclinic-II defect with two weakly coupled Si-H or Ge-H bonds. It is shown that the piezospectroscopic parameters in Table I are equal for the modes that correspond to the symmetric and asymmetric combinations of equivalent displacement coordinates of the two bonds. Usually, the theoretical stress pattern is based on first-order perturbation theory, which requires that the stress-induced frequency shifts be small compared to the separation of the modes. This requirement is not fulfilled for the modes discussed in this work and, therefore, the theory is extended to include second-order effects.

A. Basic model

The experimental results presented in Sec. IV indicate that the defect contains two equivalent Si-H or Ge-H bonds and has monoclinic-II symmetry. Thus, the two bonds transform into one another by a 180° rotation around a ⟨100⟩ axis. A simple model containing such two bonds is shown in Fig. 9. The local vibrational modes of hydrogen in silicon and germanium are effectively decoupled from the collective vibrations of the host lattice. Consequently, the local modes of our defect may be described by the coupled oscillations of two individual Si-H or Ge-H bonds. Each bond has three vibrational degrees of freedom, corresponding to a bond-stretch and two perpendicular bond-bend vibrations. Let the displacement coordinate that describe the stretching of the ith bond be denoted r_i and those describing the angular vibrations of the bond be denoted α_i and β_i (see Fig. 9). In principle, the local mode frequencies may be determined from the eigenvalues of the Hamiltonian:

$$\hat{H} = \hat{T}_{r_1} + \hat{T}_{\alpha_1} + \hat{T}_{\beta_1} + \hat{T}_{r_2} + \hat{T}_{\alpha_2} + \hat{T}_{\beta_2} + \hat{V}(r_1, \alpha_1, \beta_1, r_2, \alpha_2, \beta_2), \quad (1)$$

where $\hat{T}_{\xi_i}$ is the kinetic-energy operator corresponding to the displacement coordinate ξ_i and $\hat{V}$ is the potential-energy operator for the complex. At this point, a few clarifying remarks about our choice of coordinates are appropriate. The coordinates for the ith bond are chosen so that no cross terms coupling r_i, α_i, and β_i appear in the second-order Taylor expansion of $\hat{V}$ around the point of zero displacements. In other words, r_i, α_i, and β_i would be proportional to the normal coordinates of the ith bond in a situation where the

displacement coordinates of the other bond were fixed at zero. With this choice, the coordinates may be divided into three sets of equivalent coordinates $\{r_1,r_2\}$, $\{\alpha_1,\alpha_2\}$, and $\{\beta_1,\beta_2\}$, which are closed under the symmetry operations of the C_2 group.

In the following, we shall neglect all terms in the potential energy $\hat{V}$, which couple inequivalent coordinates, i.e., coordinates from different sets. In addition, we assume that the coupling between a pair of equivalent coordinates is dominated by the quadratic term. With these assumptions, the six-dimensional problem in Eq. (1) is reduced to three two-dimensional problems, each with a Hamiltonian of the type

$$\hat{H}_\xi=\hat{T}_{\xi_1}+\hat{T}_{\xi_2}+\hat{V}_\xi(\xi_1)+\hat{V}_\xi(\xi_2)+f_{12}^\xi\xi_1\xi_2, \quad \xi\in\{r,\alpha,\beta\}. \tag{2}$$

Here $\hat{V}_\xi$ denotes a single-coordinate potential for one of the two equivalent bonds and f_{12}^ξ is the harmonic coupling constant. It may be noted that all anharmonic terms, which depend only on a single displacement coordinate ξ_i, are included in $\hat{H}_\xi$ through $\hat{V}_\xi$. Such terms are known to give a significant contribution to the local mode frequencies of hydrogen in silicon and germanium.[14]

From each set of equivalent coordinates $\{\xi_1,\xi_2\}$, two symmetry coordinates $\xi_A=(\xi_1+\xi_2)/\sqrt{2}$ and $\xi_B=(\xi_1-\xi_2)/\sqrt{2}$ can be formed that transform like the respective irreducible representations A and B of the C_2 point group. The Hamiltonian $\hat{H}_\xi$ in Eq. (2) gives rise to an A mode and a B mode with normal coordinates proportional to ξ_A and ξ_B. Thus, the two modes associated with each set of equivalent coordinates correspond to a symmetric (ξ_A) and an asymmetric (ξ_B) combination of displacement coordinates.

The couplings between the coordinates that belong to two inequivalent sets may be neglected provided that the frequency differences between modes of the different sets are much larger than the frequency shifts induced by the couplings. This condition is obviously fulfilled for stretch and bend modes, whereas the decoupling of inequivalent bend modes is less clear. However, only two bend modes $\sim 5\ \mathrm{cm}^{-1}$ apart are observed in both silicon and germanium. Moreover, the substitution of one of the hydrogen atoms with deuterium gives rise to one additional bend mode close to the mean frequency of the two original modes. Finally, the uniaxial stress data show that the two bend modes in silicon have different symmetry. These observations strongly suggest that the two bend modes represent the symmetric and asymmetric combination of either $\{\alpha_1,\alpha_2\}$ or $\{\beta_1,\beta_2\}$. If the observed splitting between the two modes represents a typical coupling term between angular coordinates, the coupling with other bend modes would be insignificant, unless their frequencies deviate from those of the doublet by only a few times the observed splitting. The fact that no other modes are observed within this range indicates that the assumption made above is reasonable.

The frequency splitting observed between the A and the B modes of equivalent coordinates are two or three orders of magnitude smaller than the mode frequencies. Therefore, the coupling term $f_{12}^\xi\xi_1\xi_2$ in Eq. (2) may be treated by perturbation theory. The zero order eigenstates can be chosen to have the form $|n_1,n_2\rangle=|n_1\rangle_1|n_2\rangle_2$, where $|n\rangle_i$ is a normalized eigenstate of the one-dimensional Hamiltonian: $\hat{H}_\xi^i=\hat{T}_{\xi_i}+\hat{V}_\xi(\xi_i)$. The quantum number n is chosen to be a nonnegative integer in such a way that the energy of the state increases with increasing n. Since we are observing fundamental transitions, only the ground state ($n_1+n_2=0$) and the singly excited states ($n_1+n_2=1$) are of interest. To zeroth order, the $|1,0\rangle$ and $|0,1\rangle$ states are degenerate, but the coupling will imply a splitting into an $|A\rangle$ and a $|B\rangle$ state. Therefore, we apply a basis that reflects this symmetry, i.e.,

$$|A,0\rangle=|0,0\rangle \tag{3}$$

for the ground state, and for the singly excited states:

$$|A,1\rangle=\frac{1}{\sqrt{2}}(|1,0\rangle+|0,1\rangle) \quad \text{and} \quad |B,1\rangle=\frac{1}{\sqrt{2}}(|1,0\rangle-|0,1\rangle). \tag{4}$$

B. Stress pattern to first order

When uniaxial stress is introduced, the associated strain field changes the potential energies $\hat{V}_\xi(\xi_i)$ given in Eq. (2). Since this stress-induced change is small, it is usually expanded to first order in the components of the stress tensor. For the ith bond, this leads to an additional potential energy term:

$$\Delta\hat{V}_\xi^{(i)}(\sigma^{(i)})=\hbar\sum_{k,l\in\{x,y,z\}}\hat{A}_{kl}^{(i)}\sigma_{kl}^{(i)}. \tag{5}$$

In this expression $\hat{A}_{kl}^{(i)}$ denotes the klth component of the symmetric second-rank tensor $\hat{A}^{(i)}$, which represents the effect of uniaxial stress on the single coordinate potential $\hat{V}_\xi(\xi_i)$ and $\sigma_{kl}^{(i)}$ is the klth component of the stress tensor $\sigma^{(i)}$. Since the two bonds are equivalent, it is convenient to introduce bond-specific coordinate systems with orthonormal bases $\{\mathbf{e}_x^{(1)},\mathbf{e}_y^{(1)},\mathbf{e}_z^{(1)}\}$ and $\{\mathbf{e}_x^{(2)},\mathbf{e}_y^{(2)},\mathbf{e}_z^{(2)}\}$. One of these can be chosen freely, whereas the other is obtained from the first by the C_2 rotation. When the bond-specific coordinate systems are used, the relation between the expectation values of the operators $\hat{A}_{kl}^{(1)}$ and $\hat{A}_{kl}^{(2)}$ is very simple:

$${}_1\langle n|\hat{A}_{kl}^{(1)}|n'\rangle_1={}_2\langle n|\hat{A}_{kl}^{(2)}|n'\rangle_2. \tag{6}$$

As a matter of convenience we choose

$$\mathbf{e}_x^{(1)}//[100], \quad \mathbf{e}_y^{(1)}//[010], \quad \mathbf{e}_z^{(1)}//[001]. \tag{7}$$

First, one specific defect orientation with the twofold axis along [001] is considered. Then, $\mathbf{e}_x^{(1)}=-\mathbf{e}_x^{(2)}$, $\mathbf{e}_y^{(1)}=-\mathbf{e}_y^{(2)}$, and $\mathbf{e}_z^{(1)}=\mathbf{e}_z^{(2)}$, and the relation between the stress tensor in the two bond-specific systems is

$$\sigma^{(2)}=\begin{pmatrix}\sigma_{xx}^{(1)} & \sigma_{xy}^{(1)} & -\sigma_{xz}^{(1)}\\ \sigma_{xy}^{(1)} & \sigma_{yy}^{(1)} & -\sigma_{yz}^{(1)}\\ -\sigma_{xz}^{(1)} & -\sigma_{yz}^{(1)} & \sigma_{zz}^{(1)}\end{pmatrix}. \tag{8}$$

With Eqs. (5) and (8), the total stress-induced change of the Hamiltonian in Eq. (2) is

$$\Delta\hat{V}_\xi^{(1)}+\Delta\hat{V}_\xi^{(2)}=\hbar\{\hat{A}_{xx}^{(1)}+\hat{A}_{xx}^{(2)}\}\sigma_{xx}+\hbar\{\hat{A}_{yy}^{(1)}+\hat{A}_{yy}^{(2)}\}\sigma_{yy}+\hbar\{\hat{A}_{zz}^{(1)}+\hat{A}_{zz}^{(2)}\}\sigma_{zz}+2\hbar\{\hat{A}_{xy}^{(1)}+\hat{A}_{xy}^{(2)}\}\sigma_{xy}+2\hbar\{\hat{A}_{yz}^{(1)}-\hat{A}_{yz}^{(2)}\}\sigma_{yz}+2\hbar\{\hat{A}_{zx}^{(1)}-\hat{A}_{zx}^{(2)}\}\sigma_{zx}. \tag{9}$$

With the definitions in Eq. (7), the stress tensor $\sigma^{(1)}$ is given with respect to the $\langle 100\rangle$ axes of the diamond lattice and the bond indices have, therefore, been dropped in Eq. (9), i.e., $\sigma\equiv\sigma^{(1)}$. With Eqs. (3), (4), and (9), we are able to calculate the stress-induced first-order energy shifts of the ground state $|A,0\rangle$ and the singly excited states $|A,1\rangle$ and $|B,1\rangle$. The energy shifts for the transitions $|A,0\rangle\rightarrow|A,1\rangle$ and $|A,0\rangle\rightarrow|B,1\rangle$ are equal and given by

$$\Delta E_A^{(1)}=\Delta E_B^{(1)}=\hbar\Delta\omega^{(1)}=\hbar(\mathcal{A}_1\sigma_{zz}+\mathcal{A}_2\sigma_{yy}+\mathcal{A}_3\sigma_{xx}+2\mathcal{A}_4\sigma_{xy}), \tag{10}$$

where the piezospectroscopic parameters

$$\begin{aligned}\mathcal{A}_1&={}_1\langle 1|\hat{A}_{zz}^{(1)}|1\rangle_1-{}_1\langle 0|\hat{A}_{zz}^{(1)}|0\rangle_1,\\ \mathcal{A}_2&={}_1\langle 1|\hat{A}_{yy}^{(1)}|1\rangle_1-{}_1\langle 0|\hat{A}_{yy}^{(1)}|0\rangle_1,\\ \mathcal{A}_3&={}_1\langle 1|\hat{A}_{xx}^{(1)}|1\rangle_1-{}_1\langle 0|\hat{A}_{xx}^{(1)}|0\rangle_1,\\ \mathcal{A}_4&={}_1\langle 1|\hat{A}_{xy}^{(1)}|1\rangle_1-{}_1\langle 0|\hat{A}_{xy}^{(1)}|0\rangle_1\end{aligned} \tag{11}$$

have been introduced. Thus, the stress splittings of the two modes are identical.

If uniaxial stress of magnitude σ is applied along the direction defined by the unit vector $\mathbf{n}$, the components of the stress tensor are $\sigma_{ij}=\sigma\cos(\mathbf{n}\cdot\mathbf{e}_i^{(1)})\cos(\mathbf{n}\cdot\mathbf{e}_j^{(1)})$, where $i,j\in\{x,y,z\}$. For a given stress tensor σ, the stress-induced energy shift for one particular orientation of the defect is given by Eq. (10). From this particular orientation of the defect all the other defect orientations can be generated by the 24 symmetry operations $\mathbf{R}_l$ of the T_d point group. The stress-induced energy shift for the defect orientation obtained by $\mathbf{R}_l$ can also be calculated from Eq. (10) when r is replaced by

$$\sigma_l=\mathbf{R}_l^{-1}\sigma\mathbf{R}_l. \tag{12}$$

The results for stresses along [100], [111], and [110] are identical to those obtained by Kaplyanskii[18] and are given in Table I. However, the present derivation shows that the piezospectroscopic parameters are identical for the symmetric and asymmetric modes of equivalent vibrational degrees of freedom.

The probability for the transition $|A,0\rangle\rightarrow|\Gamma,1\rangle$, where $\Gamma\in\{A,B\}$, is proportional to $|\boldsymbol{\varepsilon}\cdot\mathbf{d}_\Gamma|^2$, where $\boldsymbol{\varepsilon}$ is the polarization vector of the infrared light and $\mathbf{d}_\Gamma=\langle A,0|\mathbf{d}|\Gamma,1\rangle$ is the transition matrix element of the dipole operator $\mathbf{d}$. Usually, the dipole operator is expanded to first order in the displacement coordinates ξ_1 and ξ_2. Thus,

$$\mathbf{d}=\mathbf{d}_0+\eta_\xi\xi_1\mathbf{n}_1^\xi+\eta_\xi\xi_2\mathbf{n}_2^\xi,\quad \xi\in\{r,\alpha,\beta\}, \tag{13}$$

where $\mathbf{d}_0$ is the permanent dipole moment, η_ξ is a constant denoted *the apparent charge*, and $\mathbf{n}_i^\xi$ is a unit vector that defines the orientation of the induced bond-dipole corresponding to the displacement coordinate ξ_i. Using Eqs. (3), (4), and (13), the transition matrix element is

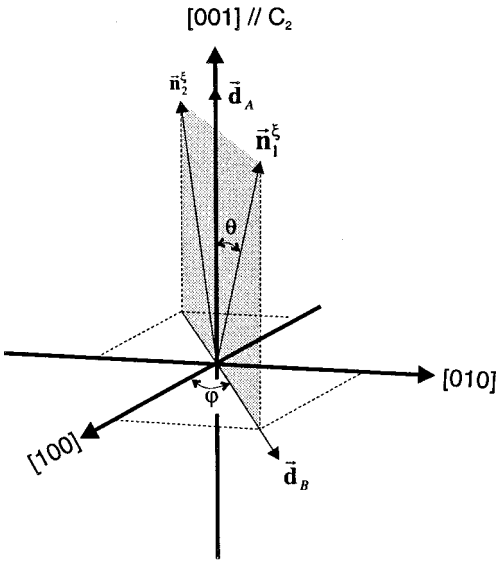

FIG. 10. Definition of the polar angle θ and azimuthal angle φ that specify the directions of the unit vectors $\mathbf{n}_1^\xi$ and $\mathbf{n}_2^\xi$ for a specific orientation of the defect. The direction of the induced dipole moments for the A mode ($\mathbf{d}_A$) and the B mode ($\mathbf{d}_B$) are also shown.

$$\mathbf{d}_\Gamma=\frac{\eta_\xi}{\sqrt{2}}\,{}_1\langle 0|\xi_1|1\rangle_1(\mathbf{n}_1^\xi\pm\mathbf{n}_2^\xi), \tag{14}$$

where *plus* corresponds to $\Gamma=A$ and *minus* to $\Gamma=B$. Again, we first consider a particular orientation of the defect with the C_2 axis along [001]. The direction of, say, $\mathbf{n}_1^\xi$ may be defined in terms of a polar angle θ and an azimuthal angle φ as shown in Fig. 10. Then $\mathbf{n}_2^\xi$ is related to $\mathbf{n}_1^\xi$ via the C_2 rotation and it also has the polar angle θ, whereas its azimuthal angle is $180°+\varphi$. Equation (14) implies that $\mathbf{d}_A$ is parallel to the C_2 axis, and $\mathbf{d}_B$ lies in the plane perpendicular to this axis and has the angle φ to the [100] direction. It is important to note that we can choose our coordinate axes in Fig. 10 and the particular orientation of the defect in such a way that $0°\leqslant\theta\leqslant 90°$ and $0°\leqslant\varphi\leqslant 45°$ (see Ref. 23). In the following we shall adopt this specific choice, which defines θ as the smallest angle to the C_2 axis and φ as the smallest angle to an $\langle 100\rangle$ axis in the plane perpendicular to the C_2 axis. It must be emphasized that the values of θ and φ obtained in this way for different types of displacement coordinates, e.g., $\xi=\alpha$ and $\xi=r$, do not in general refer to the same choice of axes nor to the same particular orientation of the defect.

The transition matrix elements corresponding to the other orientations of the defect are obtained by the symmetry operations $\mathbf{R}_l$ of the T_d point group. If the defects are distributed evenly among the different orientations, the intensity of the $|A,0\rangle\rightarrow|\Gamma,1\rangle$ transition at zero stress is proportional to the sum of the transition probabilities of all the possible defect orientations:

$$I^{(\Gamma)} \propto \sum_{\mathbf{R}_l \in T_d} |\boldsymbol{\varepsilon} \cdot (\mathbf{R}_l \mathbf{d}_\Gamma)|^2, \quad \Gamma \in \{A,B\}. \tag{15}$$

It may be noted that the mode intensity at zero stress $I^{(\Gamma)}$ is independent of the polarization of the infrared light since the sum includes all symmetry operations of the T_d point group. The ratio of the A- and B-mode intensities at zero stress can be calculated with Eqs. (14) and (15), and the result depends only on the polar angle θ:

$$\left.\frac{I^{(A)}}{I^{(B)}}\right|_{\sigma=0} = \cot^2 \theta. \tag{16}$$

Hence, the polar angle of the bond dipoles may be determined from the intensities of the absorption lines at zero stress.[24]

When uniaxial stress is applied, the intensity of an absorption line will be divided between its stress-split components. The relative intensity of a given component can be determined with Eq. (15) if the sum is restricted to those symmetry operations $\mathbf{R}_l$, which contribute to that particular component. The relative intensities of the stress components for [100], [111], and [110] stresses with the infrared light polarized parallel and perpendicular to the applied stress are given in Table I. As can be seen from the table, the relative intensities of the B mode depend on the azimuthal angle φ of the induced bond dipole moment. Thus, this angle may also be determined experimentally.

The first-order approach is only valid provided that the absolute value of the stress-induced coupling $\langle A,1|\Delta\hat{V}_\xi^{(1)} + \Delta\hat{V}_\xi^{(2)}|B,1\rangle$ is small compared to the energy splitting between $|A,1\rangle$ and $|B,1\rangle$. In the case of silicon, the observed bend modes are split by 4.9 cm^{-1} and the stretch modes by 2.9 cm^{-1}. In germanium the bend modes are split by 5.2 cm^{-1} and the stretch modes by 1.7 cm^{-1}. The maximum stress-induced frequency shifts are $\sim 1\ \mathrm{cm}^{-1}$ in silicon and $\sim 2\ \mathrm{cm}^{-1}$ in germanium (see Figs. 7 and 8) and, hence, second-order effects may be important, especially for the stretch modes in germanium.

C. Stress pattern to second order

On the basis of the previous subsection it is straightforward to include second-order effects in the analysis of the stress response. The eigenvalue problem of the Hamiltonian, given as the sum of the zero-order Hamiltonian in Eq. (2) and the stress-induced perturbation in Eq. (9), is solved in the subspaces spanned by $|A,0\rangle$ for the ground state and by $|A,1\rangle$ and $|B,1\rangle$ for the singly excited states. With this procedure[25] we find the second-order transition frequencies $\omega_\Gamma^{(2)}$:

$$\omega_A^{(2)} = \tfrac{1}{2}\ \omega_A^{(0)}(1+\sqrt{1+x^2}) + \tfrac{1}{2}\ \omega_B^{(0)}(1-\sqrt{1+x^2}) + \Delta\omega^{(1)},$$
$$\omega_B^{(2)} = \tfrac{1}{2}\ \omega_B^{(0)}(1+\sqrt{1+x^2}) + \tfrac{1}{2}\ \omega_A^{(0)}(1-\sqrt{1+x^2}) + \Delta\omega^{(1)}, \tag{17}$$

where $\omega_A^{(0)}$ and $\omega_B^{(0)}$ are the frequencies without stress, $\Delta\omega^{(1)}$ is the first-order energy shifts given in Eq. (10), and the coupling parameter x is given by

$$x = \frac{\langle A,1|\Delta\hat{V}_\xi^{(1)} + \Delta\hat{V}_\xi^{(2)}|B,1\rangle}{\frac{1}{2}\ \hbar(\omega_A^{(0)} - \omega_B^{(0)})} = \frac{2\mathcal{B}_1\sigma_{yz} + 2\mathcal{B}_2\sigma_{zx}}{\frac{1}{2}\ (\omega_A^{(0)} - \omega_B^{(0)})}. \tag{18}$$

Here, the off-diagonal piezospectroscopic parameters $\mathcal{B}_1$ and $\mathcal{B}_2$ are defined similarly to the parameters $\mathcal{A}_i, i \in \{1,2,3,4\}$, given in Eq. (11):

$$\mathcal{B}_1 = {}_1\langle 1|\hat{A}_{yz}^{(1)}|1\rangle_1 - {}_1\langle 0|\hat{A}_{yz}^{(1)}|0\rangle_1,$$
$$\mathcal{B}_2 = {}_1\langle 1|\hat{A}_{zx}^{(1)}|1\rangle_1 - {}_1\langle 0|\hat{A}_{zx}^{(1)}|0\rangle_1. \tag{19}$$

In the case of uniaxial stress in the [100] direction, all the off-diagonal stress-tensor components are zero for all orientations of the defect. According to Eq. (18) this implies that x is zero and, thus, there are no second-order contributions to the transition frequency for [100] stress. For [111] and [110] stresses, however, x is generally not zero and second-order effects may become important. This reflects the fact that uniaxial stress along a $\langle 100\rangle$ direction preserves the monoclinic-II symmetry, whereas stress in other directions reduces the symmetry of the defect to triclinic.

The transition matrix element $\mathbf{d}_\Gamma$ given in Eq. (14) is correct only in a first-order treatment. Since stress-induced coupling of the ground state to other states is neglected, the initial state of the transitions remains identical to $|A,0\rangle$. However, when $x \neq 0$ the singly excited final state $|\Gamma,1\rangle$ will be a normalized linear combination of the $|A,1\rangle$ and $|B,1\rangle$ states:

$$|\Gamma,1\rangle = t_A|A,1\rangle + t_B|B,1\rangle, \tag{20}$$

where the coefficients t_A and t_B depend on x. With this expression for $|\Gamma,1\rangle$, the transition matrix element may be calculated and we find

$$\mathbf{d}_\Gamma^{(2)} = \frac{\eta_\xi}{\sqrt{2}}\ {}_1\langle 0|\xi_1|1\rangle_1 \{(t_A + t_B)\mathbf{n}_1^\xi + (t_A - t_B)\mathbf{n}_2^\xi\}. \tag{21}$$

Now, the relative intensities of the stress-split components may be calculated as discussed in the previous subsection [see Eq. (15)]. Obviously, the intensities of the stress-split components differ from the first-order result in Table I, and they depend on the magnitude as well as on the direction of the applied uniaxial stress when second-order effects are important (i.e., $x \neq 0$). Due to this complication, we are unable to give simple analytical expressions for the intensity ratios of the stress components. However, a simulation of the line profiles at the maximum stresses attained in the [100], [111], and [110] directions is presented in the next section.

VI. ANALYSIS OF THE UNIAXIAL STRESS EXPERIMENTS

With the theoretical stress pattern of a monoclinic-II center derived in the previous section, we can perform a detailed analysis of the stress pattern observed for the 1881.8- and

1883.5-cm^{-1} lines in Ge:H and the 743.1-, 748.0-, 1986.5-, and 1989.4-cm^{-1} lines in Si:H.

A. Analysis of the Ge-H lines

In Sec. IV we showed that the Ge-H lines at 1881.8 and 1883.5 cm^{-1} represent the stretch modes of a monoclinic-II defect containing two equivalent hydrogen atoms. Hence, we can use Eq. (16) and the intensities of the two lines measured without stress to find $\theta = 45° \pm 1°$ for the Ge-H stretch modes.

As can be seen from Fig. 7, the lines at 1881.8 and 1883.5 cm^{-1} split into three components under [100] stress, and the slopes of the stress splittings for the two lines are equal within the experimental uncertainties. These observations are in accordance with the first-order stress pattern, as expected since the coupling parameter $x = 0$ for [100] stress. The experimental and theoretical (Table II) intensities of the [100]-stress components suggest that the azimuthal angle φ is close to 0°. With this angle, the first-order stress patterns for [100] (and [111]) stresses of the lines corresponding to $|A,0\rangle \rightarrow |A,1\rangle$ and $|A,0\rangle \rightarrow |B,1\rangle$ transitions differ only by a permutation of $\mathcal{A}_1$ and $\mathcal{A}_3$. Therefore, it is not possible to ascribe a specific transition to the 1881.8-or 1883.5-cm^{-1} line solely from the [100] (and [111]) stress patterns. However, the observed stress patterns for [110] stress and [001] polarization ($\boldsymbol{\varepsilon}$//[001]) are markedly different for the two lines. Only one component of the 1881.8-cm^{-1} line is observed under these conditions, whereas the 1883.5-cm^{-1} line is observed to split into two components of equal intensity (see Fig. 11). As can be seen from Table I, this strongly indicates that the line at 1881.8 cm^{-1} originates from the $|A,0\rangle \rightarrow |B,1\rangle$ transition, whereas the line at 1883.5 cm^{-1} originates from the $|A,0\rangle \rightarrow |A,1\rangle$ transition. With this identification and $\varphi \sim 0°$, the piezo-spectroscopic parameters $\mathcal{A}_1$, $\mathcal{A}_2$, and $\mathcal{A}_3$ can be determined from the [100]-stress data.

In order to understand the observed stress patterns for [111] and [110] stress and to obtain accurate values of φ and $\mathcal{A}_4$, it is necessary to include second-order effects. For instance, it is evident from Fig. 7 that the experimental stress splittings for [111] stress are different for the 1881.8- and 1883.5-cm^{-1} lines. The 1881.8-cm^{-1} line splits into two components while the 1883.5-cm^{-1} line does not split, in conflict with the first-order stress pattern. The second-order effects are taken into account with a detailed line profile analysis of the spectra measured at maximum stresses, using the second-order theory described in Sec. V C. At zero stress, the line shape of the Ge-H lines is nearly Gaussian. Since all the 24 different orientations of the defect are assumed to occur with equal probability, we assume that the 1881.8- and 1883.5-cm^{-1} lines both consist of a superposition of 24 Gaussians with equal position, amplitude, and width. When uniaxial stress is applied, the positions and relative amplitudes of the Gaussians are changed according to the second-order theory. The line positions at zero stress, the line widths, the polar angle θ, and the constant $\eta_{\xi\ 1}\langle 0|\xi_1|1\rangle_1$ are fixed at the values obtained from the line profiles at zero stress. The piezospectroscopic parameters $\mathcal{A}_1$, $\mathcal{A}_2$, $\mathcal{A}_3$, $\mathcal{A}_4$, $\mathcal{B}_1$, $\mathcal{B}_2$, and the azimuthal angle φ are treated as fitting parameters. In Fig. 12, the line profiles observed at maximum stress are compared with those corresponding to the best fit, obtained with the parameters presented in Table II. Furthermore, the second-order line splittings for uniaxial stress along [100] and [111] that correspond to the best-fit parameters are shown as solid curves in Fig. 7. It is evident that the experimental stress patterns of the Ge-H lines at 1881.8 and 1883.5 cm^{-1} are very well accounted for by the second-order stress pattern of a monoclinic-II center containing two equivalent Ge-H bonds.

TABLE II. The piezo-spectroscopic parameters (in cm^{-1}/GPa), the polar angles and the azimuthal angles corresponding to the best-fit curves shown in Figs. 7, 8, and 12. See text for further details.

Mode frequency	Si:H bend 743.1 cm^{-1} 748.0 cm^{-1}	Si:H stretch 1986.5 cm^{-1} 1989.4 cm^{-1}	Ge:H stretch 1881.8 cm^{-1} 1883.5 cm^{-1}
$\mathcal{A}_1$	-0.3 ± 0.3[a]	0.18 ± 0.19[a]	2.2 ± 0.2[b]
$\mathcal{A}_2$	1.4 ± 0.4[a]	0.9 ± 0.3[a]	0.9 ± 0.2[b]
$\mathcal{A}_3$	0.8 ± 0.3[a]	1.4 ± 0.2[a]	3.6 ± 0.2[b]
$\mathcal{A}_4$	0.6 ± 0.2[b]	0.9 ± 0.2[b]	1.0 ± 0.1[b]
$\mathcal{B}_1$			-1.4 ± 0.2[b]
$\mathcal{B}_2$			1.0 ± 0.2[b]
θ	$43° \pm 2°$	$48° \pm 1°$	$45° \pm 1°$
φ	$0° \pm 8°$		$3° \pm 5°$

[a]Measured at 4.2 K.

[b]Measured at 77 K.

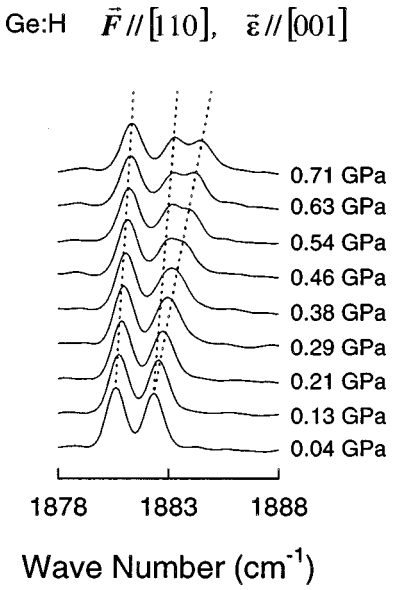

FIG. 11. The stress response of the 1881.8- and 1883.5-cm^{-1} lines in Ge:H measured at 77 K with stress along [110] and [001] polarization. The dotted lines indicate the stress-induced splittings.

B. Analysis of Si-H lines

The polar angle for the Si-H stretch modes is readily found to be $\theta = 48° \pm 1°$ from Eq. (16) and the experimental intensities of the 1986.5 and 1989.4 cm^{-1} lines at zero stress. If we assume that the Si-H lines at 743.1 and 748.0 cm^{-1} correspond to the symmetric and asymmetric combination of

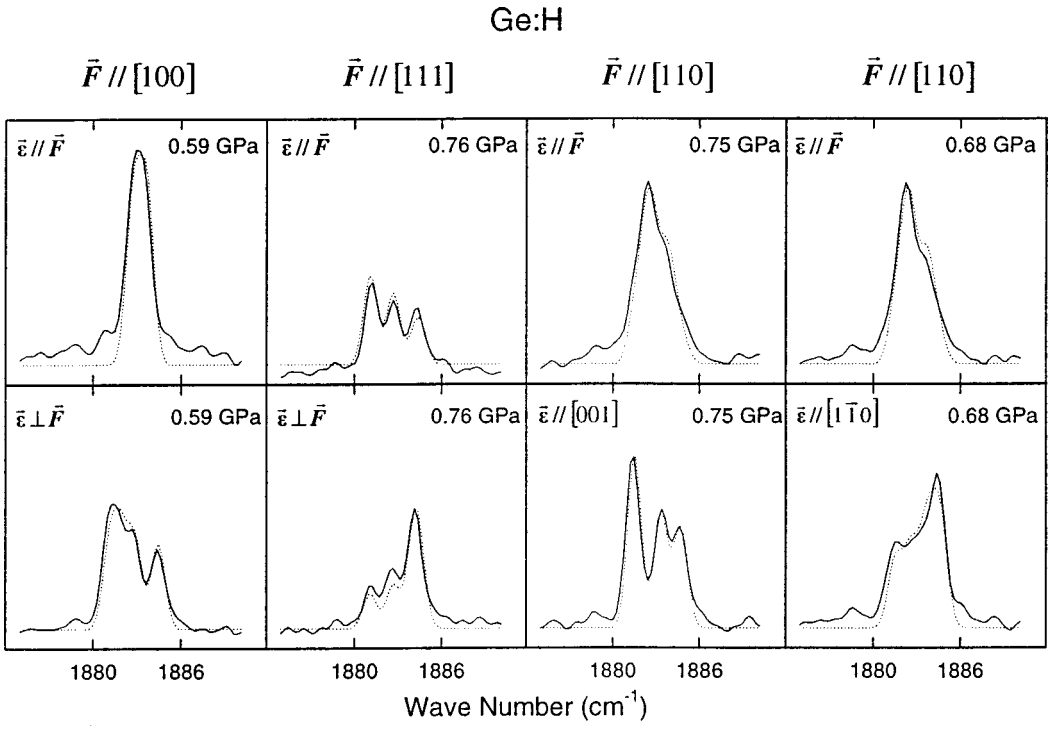

FIG. 12. The profiles of the 1881.8- and 1883.5-cm^{-1} lines in Ge:H at the maximum stresses obtained. The solid curves are the measured spectra and the dotted curves represent the line profiles obtained with the best-fit parameters presented in Table II. The spectra were measured at 77 K.

two equivalent angular degrees of freedom, the polar angle $\theta = 43° \pm 2°$ is obtained for the two bend modes.

As mentioned in Sec. IV, the Si-H lines at 743.1, 748.0, 1986.5, and 1989.4 cm^{-1} are rather insensitive to uniaxial stress and the individual stress components are not well resolved. In fact, the splitting at zero stress is at least three times larger than the experimental stress-induced shifts at maximum stress. We expect, therefore, second-order effects to be negligible for these lines and analyze the observed stress pattern with the first-order expressions of Table I.

For stress along [110] and [001] polarization, only one component is observed for the 1986.5-cm^{-1} line whereas the line at 1989.4 cm^{-1} splits into two components of about equal intensity (see Fig. 13). If we assume that the 1989.4-cm^{-1} line corresponds to the $|A,0\rangle \rightarrow |B,1\rangle$ transition, then the size of the splitting is $|1/2(\mathcal{A}_2 - \mathcal{A}_3)\sigma|$ and the azimuthal angle is $\varphi \sim 45°$, according to Table I. Then, the 1989.4-cm^{-1} line should also split into two components with about equal intensity for stress along [100] and parallel polarization. The splitting of these two components should be $|(\mathcal{A}_2 - \mathcal{A}_3)\sigma|$, i.e., twice the splitting observed for [110] stress and [001] polarization and should, therefore, easily be resolved. However, with [100] stress no such splitting is observed for the 1989.4-cm^{-1} line and, thus, it cannot represent the $|A,0\rangle \rightarrow |B,1\rangle$ transition. On the other hand, the stress pattern of the 1989.4-cm^{-1} line agrees with that of the $|A,0\rangle \rightarrow |A,1\rangle$ transition, if the parameters $\mathcal{A}_2$ and $\mathcal{A}_3$ are about equal. Moreover, the stress pattern for the line at 1986.5-cm^{-1} is consistent with the $|A,0\rangle \rightarrow |B,1\rangle$ transition. Hence, we ascribe the 1986.5- and 1989.4-cm^{-1} lines to the $|A,0\rangle \rightarrow |B,1\rangle$ and $|A,0\rangle \rightarrow |A,1\rangle$ transitions, respectively. Due to the small difference between $\mathcal{A}_2$ and $\mathcal{A}_3$, the azimuthal angle φ cannot be determined with a reasonable accuracy, but a value close to zero is consistent with the experimental data also in this case. With $\varphi = 0°$, the theoretical first-order frequency shifts of Table I are fitted to those observed for [100] stress. The intensity-weighted averages of the theoretical frequency shifts are used when the individual components are unresolved experimentally. The best-fit pa-

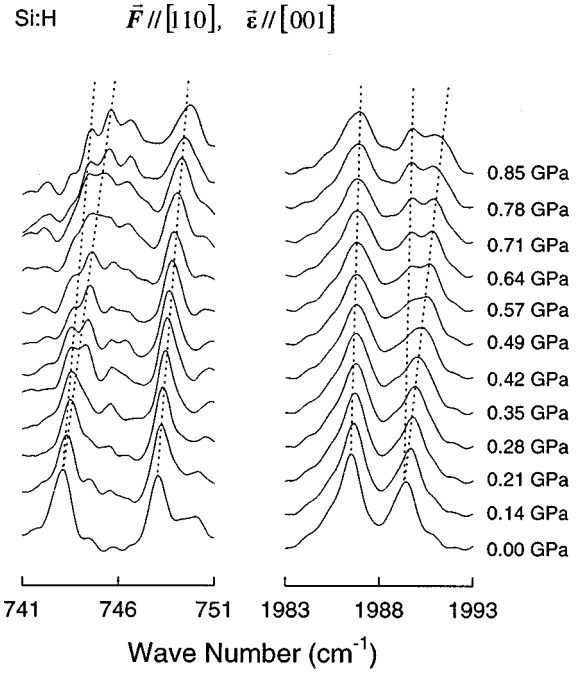

FIG. 13. The stress response of the 743.1-, 748.0-, 1986.5-, and 1989.4-cm^{-1} lines in Si:H measured at 77 K with stress along [110] and [001] polarization. The dotted lines indicate the stress-induced splittings.

rameters $\mathcal{A}_1$, $\mathcal{A}_2$, and $\mathcal{A}_3$ for the Si-H stretch modes are presented in Table II and the solid lines in Fig. 8 correspond to the theoretical frequency shifts with these parameters.

The symmetry of the modes that gives rise to the lines at 743.1 and 748.0 cm^{-1} may be determined by the procedure applied just above. The 743.1 cm^{-1} line splits into two components for stress along [110] and [001] polarization while a single component only is observed for the line at 748.0 cm^{-1} (see Fig. 13). Hence, if the 743.1-cm^{-1} line represents the $|A,0\rangle \rightarrow |B,1\rangle$ transition, two components with the same intensity ratio and twice the splitting observed for [110] stress and [001] polarization should be observed for stress along [100] and parallel polarization. However, such a splitting is not observed (see Fig. 8), and the 743.1-cm^{-1} line is assigned to the $|A,0\rangle \rightarrow |A,1\rangle$ transition. Moreover, the stress pattern for the 748.0-cm^{-1} line is consistent with that expected for the $|A,0\rangle \rightarrow |B,1\rangle$ transition. The values of the best-fit parameters $\mathcal{A}_1$, $\mathcal{A}_2$, and $\mathcal{A}_3$ are given in Table II. The two components observed for the 748.0-cm^{-1} line for stress along [100] and parallel polarization have almost equal intensities. From this the azimuthal angle is estimated to be $\varphi = 0° \pm 8°$.

On this basis, we assign the 743.1- and 748.0-cm^{-1} lines, respectively, to the excitations of the symmetric and asymmetric Si-H bend modes associated with equivalent angular displacement coordinates.

VII. DISCUSSION

The experiments show that the Ge-H lines at 700.3, 705.5, 1881.8, and 1883.5 cm^{-1} represent local vibrational modes of a defect with two equivalent, weakly coupled Ge-H bonds. The response of the Ge-H lines at 1881.8 and 1883.5 cm^{-1} to uniaxial stress is in excellent agreement with the theoretical second-order stress pattern of the $|A,0\rangle \rightarrow |B,1\rangle$ and $|A,0\rangle \rightarrow |A,1\rangle$ transitions of a monoclinic-II center. The polar angle of the stretch modes is found to be $\theta = 45° \pm 1°$ and the azimuthal angle is $\varphi = 3° \pm 5°$.

Likewise, the 743.1-, 748.0-, 1986.5- and 1989.4-cm^{-1} lines in Si:H correspond to local vibrational modes of a monoclinic-II defect that contains two equivalent and weakly coupled Si-H bonds. The ordering of the Si-H stretch modes is identical to that of the Ge-H stretch-modes i.e., the 1986.5-cm^{-1} line corresponds to the $|A,0\rangle \rightarrow |B,1\rangle$ transition and the 1989.4-cm^{-1} line to the $|A,0\rangle \rightarrow |A,1\rangle$ transition. The ordering of the Si-H bend modes, however, is reversed compared the stretch modes. The polar angle for the Si-H stretch modes is found to be $\theta = 48° \pm 1°$ and for the Si-H bend modes $\theta = 43° \pm 2°$. The azimuthal angle of the stretch modes cannot be determined, whereas $\varphi = 0° \pm 8°$ for the bend modes.

The frequencies of the four Ge-H and four Si-H modes scale very accurately with those of the germane and silane molecules. Moreover, the physical properties of the defect that gives rise to the four modes are essentially identical in germanium and in silicon. This establishes that the set of four modes originate the same defect in the two materials.

The angles θ and φ specify the direction of the unit vectors $\mathbf{n}_1^{\xi}$, $\xi \in \{\alpha,\beta,r\}$, i.e., the direction of the induced dipole moment associated with a displacement of the type ξ_1 of the first bond. For stretch modes, we expect the bond moment to be directed along the Ge-H (or Si-H) bond and, consequently, θ and φ of the stretch modes specify the direction of this bond. Hence, we can determine the smallest angle between the bond and the C_2 axis (θ) and the smallest angle between the projection of the bond onto the plane perpendicular to the C_2 axis and a $\langle 100 \rangle$ direction in this plane (φ). The values of θ and φ obtained for the Ge- H or Si-H stretch modes imply that with the C_2 axis along [001], the two Ge-H or Si-H bonds are nearly aligned with the [011] and [01$\bar{1}$] directions. The two Ge-H or Si-H bonds are nearly perpendicular. This suggests that the dynamical coupling of the stretch vibrations of the two bonds is weak, and provides an intuitive explanation for the very small frequency splitting of the two stretch modes.

Moreover, we can obtain information on the nature of the Si-H bend modes at 743.1 and 748.0 cm^{-1}. If we assume that $\mathbf{n}_1^{\xi}$ is parallel to the direction defined by an infinitesimal increase in the displacement coordinate ξ_1, then $\mathbf{n}_1^{\alpha}$, $\mathbf{n}_1^{\beta}$, and $\mathbf{n}_1^{r}$ are mutually perpendicular. However, the values of θ and φ for the Si-H bend and stretch modes presented in Table II do not define perpendicular vectors. As mentioned in Sec. VI, this reflects that these values do not refer to the same choice of coordinate system and/or defect orientation.[23] If the polar angle for the Si-H stretch modes is fixed at $\theta = 48° \pm 1°$ and, moreover, we require that $\mathbf{n}_1^{\xi}$ of the observed bend modes is perpendicular to $\mathbf{n}_1^{r}$, then the only solution to Eq. (16) for the observed bend-modes is $\theta = 137° \pm 2°$. We can now calculate the difference in azimuthal angle of the stretch and bend modes to be $\Delta\varphi = 15° \pm 17°$, which is consistent with the values $\varphi = 0° \pm 8°$ for the bend modes and $\varphi \sim 0°$ for the stretch modes. Thus, the bend and stretch modes have nearly the same azimuthal angle, which implies that the bend modes are associated with the symmetric and asymmetric combinations of angular displacements almost in the plane spanned by the C_2 axis and the Si-H bond, i.e., the α coordinates defined in Fig. 9.

The simplest defect that is consistent with all our findings is the IH_2 defect shown in Fig. 1(b). As can be seen from the figure, this defect contains two nearly perpendicular and equivalent Si-H bonds that are almost aligned with the [011] and [01$\bar{1}$] directions and has a C_2 axis parallel to the [001] direction. On this basis, we assign the four Ge-H modes at 700.3, 705.5, 1881.8, and 1883.5 cm^{-1} and the four Si-H modes at 743.1, 748.0, 1986.5, and 1989.4 cm^{-1} to the IH_2 defect.

It may be argued that the four modes could just as well originate from a hydrogen-impurity or a hydrogen-vacancy complex. However, the concentration of impurities (apart from hydrogen) in our samples is too low to account for the strong absorption observed. Hence, hydrogen-impurity complexes can be ruled out. With respect to hydrogen-vacancy complexes, we note that the atoms surrounding a vacancy-type defect in silicon and germanium are three-fold coordinated and have a dangling bond that points in a $\langle 111 \rangle$ direction. Hydrogen may saturate this dangling bond,[8] and the resulting Si-H or Ge-H bond will essentially be aligned with the $\langle 111 \rangle$ direction. Since this is inconsistent with the $\langle 110 \rangle$ orientation of the Si-H or Ge-H bonds, which we observe, this possibility can also be ruled out.

VIII. *AB INITIO* CALCULATIONS

To provide further support to the assignments made in the previous section, the structure and local vibrational modes of IH_2 in silicon and germanium are calculated with *ab initio* theory. In addition, the structure and the local vibrational modes of IH are calculated together with the structure of the self-interstitial in both silicon and germanium.

A. Theoretical method

The *ab initio* calculations are performed with the local-density-functional cluster method AIMPRO (Ref. 26) on 132–134 atom clusters $X_{72}H_{60+n}$ where X is a host atom (either Si or Ge) and $n \in \{0,1,2\}$. One host atom and n hydrogen atoms are added to a tetrahedral hydrogen-terminated $X_{71}H_{60}$ cluster representing the perfect crystal. The following basis set for the wave functions is used: eight Gaussian s and p orbitals with different widths centered on each of the innermost six host atoms, a fixed linear combination of these eight Gaussian s and p orbitals for the remaining host atoms, four Gaussian s and p orbitals with different widths for the n hydrogen atoms in the core of the defect, a fixed combination of three Gaussian s and p orbitals each for hydrogen at the cluster surface and, finally, additional basis functions are placed at the centers of the bonds between the $6+n$ atoms in the defect core. The self-consistent energy and the forces on the atoms are calculated and all 72 host atoms and n hydrogen atoms at the defect core are allowed to relax until the minimum-energy configuration is obtained. The hydrogen atoms at the surface are fixed during this procedure. The minimization is performed with a conjugate gradient algorithm. The second derivatives of the energy between the $6+n$ central atoms are calculated directly, while the derivatives between the remaining atoms are found from a Musgrave Pople potential given previously.[26] Then, the dynamical matrix of the cluster is constructed, and the local vibrational modes along with their isotope shifts are calculated.

B. The self-interstitial (I)

For the isolated self-interstitial in its neutral charge state and with zero spin, we find a number of configurations close in energy. Here we shall concentrate on the two with lowest energy. In silicon, the most stable defect is the ⟨110⟩ split-interstitial illustrated in Fig. 1(a). Previous studies have also found this structure to possess the lowest energy.[2–6] To our knowledge, the self-interstitial in germanium has not previously been investigated theoretically. Also in this material we find the most stable configuration to be the ⟨110⟩ split.

The other configuration of interest is a ⟨100⟩ split, i.e., it consists of two atoms that share a lattice site and are split in the ⟨100⟩ direction. This configuration is similar to that of the carbon interstitial.[27,28] The point group of the unrelaxed defect is D_{2d} (tetragonal), and it possesses a partially occupied e (doublet) level lying around midgap. Hence, the structure is a candidate for a Jahn-Teller distortion, which lifts the tetragonal symmetry and splits the partially occupied e level into singlets. The relaxation on the [100] split-interstitial results in a large movement of one of the two core atoms along the [011] direction so that the structure ends up with C_{1h} (monoclinic-I) symmetry. In silicon and germanium, this configuration has, respectively, 0.31 eV and 0.51 eV higher energy than the ⟨110⟩ split interstitial.

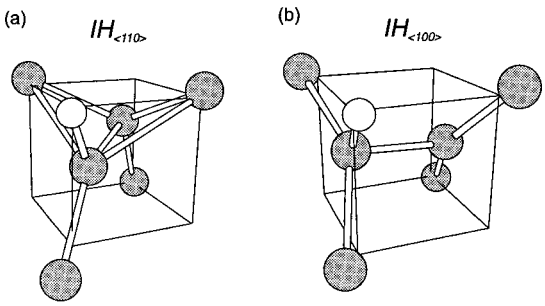

FIG. 14. The calculated structure of (a) $IH_{\langle 110\rangle}$ and (b) $IH_{\langle 100\rangle}$ in silicon and germanium. The shaded spheres are silicon or germanium, whereas the white spheres are hydrogen.

C. The IH defect

The starting configurations are ⟨110⟩ and ⟨100⟩ split-interstitials with a hydrogen atom attached to one of the two equivalent core atoms. When the relaxation is carried out, the two starting configurations end up in different configurations that both have C_{1h} (monoclinic-I) symmetry [see Figs. 14(a) and 14(b)]. In both materials, the energy difference between the two configurations is small, with the ⟨100⟩ orientation $IH_{\langle 100\rangle}$ being favored by 0.24 eV in silicon over $IH_{\langle 110\rangle}$ whereas the two configurations are degenerate in germanium. The silicon result is in disagreement with recent *ab initio* calculations[6] where a structure close to our $IH_{\langle 110\rangle}$ was found to be the ground state configuration. However, the $IH_{\langle 100\rangle}$ structure is similar to that found previously by Deák *et al.* using semiempirical methods.[9] The calculated hydrogen-related local vibrational mode frequencies and the isotope shifts of $IH_{\langle 100\rangle}$ and $IH_{\langle 110\rangle}$ are given in Tables III and IV. Also presented in these tables are the polar and azimuthal angles for the displacement of the Si-H or Ge-H bond for each of the modes. The displacements associated with the

TABLE III. The calculated local vibrational modes of $IH_{\langle 100\rangle}$ in silicon and germanium. The angles θ and φ specify the direction of the bond displacement associated with the modes and the column denoted Freq. gives the frequencies of the modes in cm^{-1}. The frequencies of $ID_{\langle 100\rangle}$ are also given.

		Si $IH_{\langle 100\rangle}$		$ID_{\langle 100\rangle}$
Mode	θ	φ	Freq.	Freq.
A'	45.2°	7.33°	2166.9	1556.3
A''	135.0°	0°	743.8	578.5
A'	93.6°	93.6°	724.2	578.8
		Ge $IH_{\langle 100\rangle}$		$ID_{\langle 100\rangle}$
Mode	θ	φ	Freq.	Freq.
A'	45.1°	5.07°	2079.7	1478.9
A'	92.5°	92.5°	734.5	521.0
A''	135°	0°	729.9	517.8

TABLE IV. The calculated local vibrational modes of $IH_{\langle 110\rangle}$ in silicon and germanium. The angles θ and φ specify the direction of the bond displacement associated with the modes and the column denoted Freq. gives the frequencies of the modes in cm^{-1}. The frequencies of $ID_{\langle 110\rangle}$ are also given.

		Si $IH_{\langle 110\rangle}$		$ID_{\langle 110\rangle}$
Mode	θ	φ	Freq.	Freq.
A'	36.4°	45.0°	2190.8	1574.1
A'	126.4°	45.0°	882.0	649.7
A''	90.0°	135.0°	749.0	539.3
		Ge $IH_{\langle 110\rangle}$		$ID_{\langle 110\rangle}$
Mode	θ	φ	Freq.	Freq.
A'	43.0°	45.0°	2073.7	1474.8
A'	133.0°	45.0°	800.5	567.3
A''	90.0°	135.0°	762.2	541.4

stretch modes deviate by less than 2° from the direction of the bond. For $IH_{\langle 110\rangle}$ in silicon and germanium and for $IH_{\langle 100\rangle}$ in germanium, the bend modes with the highest frequency are associated with the angular vibrations in the mirror plane of the defect, whereas the low-frequency bend modes correspond to vibrations perpendicular to this plane. For $IH_{\langle 100\rangle}$ in silicon, the ordering of the bend modes is reversed.

So far, there have been no experimental reports of these modes. The stretch-mode frequencies in silicon at 2166.9 cm^{-1} for $IH_{\langle 100\rangle}$ and 2190.8 cm^{-1} for $IH_{\langle 110\rangle}$ are considerably higher than the 1870 cm^{-1} found previously for the $\langle 110\rangle$ configuration in Ref. 6, but agrees reasonably with the unscaled value 2217 cm^{-1} for the $\langle 100\rangle$ configuration found in Ref. 9.

D. The IH_2 defect

When two hydrogen atoms are added to the $\langle 100\rangle$ and the $\langle 110\rangle$ split-interstitials with the silicon or germanium atoms kept fixed, the minimum-energy configurations have C_2 (monoclinic-II) and C_{2v} (orthorhombic-I) symmetry, respectively. If the relaxation is carried out maintaining these symmetries, then the relaxed $\langle 100\rangle$ structure in silicon has 2.56 eV lower energy than the relaxed $\langle 110\rangle$ structure. In germanium, the corresponding energy difference is 2.18 eV. If, however, the full relaxation is carried out without any symmetry constraint, then the $\langle 110\rangle$ defect rotates into the one derived from the $\langle 100\rangle$ orientation. The structure of the ground-state configuration of IH_2 is shown in Fig. 1(b). The structure in both silicon and germanium is very similar to those give previously in silicon.[6,9] Calculations performed in a large cluster ($Si_{183}H_{118}$) revealed that the energy of the IH_2+I defects is about 0.6 eV lower than that of two $IH_{\langle 100\rangle}$ defects. Therefore, the $IH_{\langle 100\rangle}$ defect may be suppressed in either material, due to the preferential formation of the fully hydrogenated defect. The calculated local vibrational mode frequencies of IH_2, IHD, and ID_2 are presented in Table V together with the polar and azimuthal angles of the mode displacements for one of the Si-H or Ge-H bonds. The stretch frequencies for IH_2 are found to lie significantly below those calculated for vacancy-hydrogen defects, which were in turn about 7% higher than the experimental values.[8]

TABLE V. The calculated local vibrational modes of IH_2 in silicon and germanium. The angles θ and φ specify the direction of the displacement of one of the bonds for each mode and the column denoted Freq. gives the frequencies of the modes in cm^{-1}. The frequencies of ID_2 and IHD are also given. The observed frequencies are given in parentheses.

			Si IH_2	ID_2	IHD
Mode	θ	φ	Freq.	Freq.	Freq.
A	45.9°	9.49°	2144.7 (1989.4)	1540.2 (1448.2)	2143.8 (1987.8)
B	46.1°	9.79°	2142.9 (1986.5)	1539.9 (1446.1)	1540.1 (1447.3)
A	129.1°	47.3°	774.7 (748.0)	590.2	771.4 (745.7)
B	127.9°	51.1°	768.1 (743.1)	582.6	727.3
B	67.7°	122.9°	736.4	564.3	589.8
A	69.8°	120.3°	717.5	555.0	579.8
			Ge IH_2	ID_2	IHD
Mode	θ	φ	Freq.	Freq.	Freq.
A	46.0°	8.30°	2056.7 (1883.5)	1462.5 (1359.0)	2055.1 (1882.8)
B	45.7°	8.47°	2053.3 (1881.8)	1460.1 (1357.6)	1461.3 (1358.4)
B	135.4°	15.7°	787.4 (705.5)	558.8	784.9 (~703)
A	132.0°	37.6°	784.7 (700.3)	555.7	712.4
A	74.5°	113.7°	725.0	514.7	555.9
B	86.5°	101.9°	694.6	493.1	503.7

This suggests that primarily the p orbitals of the two innermost silicon and germanium atoms contribute to the bonding of hydrogen. The calculated stretch-mode frequencies are 8% too high in silicon and 9% too high in germanium compared to the observed frequencies. Such deviations are typical for the theoretical method, and may be ascribed to the overbinding caused by density-functional theory and to anharmonic effects. In both silicon and germanium, the theory predicts that for the stretch modes, the A mode has higher frequency than the B mode, in agreement with our observations. The calculated splittings of the two stretch modes of IH_2 (ID_2) are small and are 1.8 (0.3) cm^{-1} in silicon and 3.4 (2.4) cm^{-1} in germanium. These agree roughly with the observed splittings of 2.9 (2.1) cm^{-1} and 1.7 (1.4) cm^{-1} in the two materials. Hence, the small splitting of the stretch modes is reproduced by the calculations. Moreover, the calculated stretch-frequencies of IHD deviate by less than 0.1 cm^{-1} from the average frequency of the respective two stretch modes of IH_2 and ID_2. Hence, the calculated isotopic shifts for the stretch modes are in excellent agreement with experiment. The directions of the bond displacements for the two stretch modes are equal and deviate by less than 2° from the directions of the bonds. In silicon, the polar angle is $\theta = 46°$ and the azimuthal angle $\varphi = 10°$, and in germanium $\theta = 46°$ and $\varphi = 8°$. These θ and φ values are in excellent agreement with the experimental results and strongly support our assignments.

For IH_2, four bend modes are predicted at 717.5, 736.4, 768.1, and 774.7 cm^{-1} in silicon and at 694.6, 725.0, 784.7, and 787.4 cm^{-1} in germanium. The calculated frequencies of the hydrogen-related bend modes of the IHD defect are 727.3 and 771.4 cm^{-1} in silicon and 712.4 and 784.9 cm^{-1} in germanium. Hence, IHD is predicted to give rise to a bend-mode between the two high-frequency (and the two low-frequency) bend modes of IH_2. Also this is in agreement with the observations both in silicon and germanium. The calculated Si-H bend-modes at 768.1 and 774.7 cm^{-1} (717.5 and 736.4 cm^{-1}) are associated with displacements in the directions specified by the polar angle $\theta \approx 129°$ and the azimuthal angle $\varphi \approx 49°$ ($\theta \approx 69°$ and $\varphi \approx 122°$). The calculated displacement vectors for the high-frequency modes deviate substantially from those obtained experimentally ($\theta = 137° \pm 2°$ and $\varphi = 0° \pm 8°$). In addition, the calculations show that the 768.1-cm^{-1} mode is a B mode, whereas the 774.7-cm^{-1} mode is an A mode, i.e., the ordering is reversed compared to the experimental results. The explanation for these discrepancies is probably that the calculations underestimate the difference in frequency between the set of high-frequency and the set of low-frequency bend modes. Two observations support this explanation. Firstly, only two bend modes are observed in both materials although the lower limit for detection is ~ 600 cm^{-1}. This gives a lower limit on the separation of the two sets of modes at ~ 140 cm^{-1} (~ 100 cm^{-1}) in silicon (germanium), which is considerably larger than the ~ 30 cm^{-1} (~ 60 cm^{-1}) separation calculated. The calculated separation is twice as big in germanium as in silicon. If our explanation for the discrepancies is correct we will, therefore, expect that the calculated normal modes of IH_2 in germanium are in better agreement with the observations. It should be stressed that this argument relies heavily on the fact that the calculated structures of the IH_2 defect in silicon and germanium are almost identical. The ordering of the calculated bend modes of IH_2 in germanium is different than that of IH_2 in silicon (see Table V) and in total agreement with the observations for the Si-H bend modes. Moreover, the calculated polar and azimuthal angles of the bond displacements for the two high-frequency bend modes in germanium are qualitatively consistent with those observed. These considerations support our explanation of the discrepancies.

IX. CONCLUSION

The infrared absorption lines at 743.1, 748.0, 1986.5, and 1989.4 cm^{-1} in Si:H and at 700.3, 705.5, 1881.8, and 1883.5 cm^{-1} in Ge:H originate from a defect containing two equivalent and weakly coupled Si-H or Ge-H bonds. The symmetry of the defect is monoclinic-II corresponding to a C_2 point group. The two Si-H or Ge-H bonds are almost perpendicular and their directions deviate only by a few degrees from $\langle 110 \rangle$. The structure of IH_2 in silicon and germanium calculated by *ab initio* theory is in excellent agreement with the information deduced experimentally, confirming the identity of the defects as the fully hydrogenated self-interstitial. Moreover, the small frequency splittings between the two stretch and the two bend modes are reproduced by the theoretical calculations together with the isotopic shifts. The calculated frequencies deviate by 8–9 % H from those observed, which is typical for the method. Based on these findings, we conclude that the Si-H modes at 743.1, 748.0, 1986.5, and 1989.4 cm^{-1} and the Ge-H modes at 700.3, 705.5, 1881.8, and 1883.5 cm^{-1} originate from the IH_2 defect.

ACKNOWLEDGMENTS

This work has been supported by the Danish National Research Foundation through Aarhus Center for Advanced Physics (ACAP). We thank the HPCI for an allocation of computer time on the Cray T3D at Edinburgh and the SP2 at Daresbury. S.Ö. thanks NFR and TFR in Sweden for financial support and also PDC at KTH for computer time on the SP2.

[1] G. D. Watkins, in *Materials Science and Technology*, edited by W. Schröter (VCH, Weinheim, 1991), Vol. 4.

[2] Y. Bar-Yam and J. D. Joannopoulos, Phys. Rev. Lett. **52**, 1129 (1984).

[3] R. Car, P. J. Kelly, A. Oshiyama, and S. T. Pantelides, Phys. Rev. Lett. **54**, 360 (1985).

[4] P. E. Blöchl, E. Smargiassi, R. Car, D. B. Laks, W. Andreoni, and S. T. Pantelides, Phys. Rev. Lett. **70**, 2435 (1993).

[5] D. J. Chadi, Phys. Rev. B **46**, 9400 (1992).

[6] C. G. Van de Walle and J. Neugebauer, Phys. Rev. B **52**, R14 320 (1995).

[7] Y. J. Chabal, Physica B **170**, 447 (1991).

[8] B. Bech Nielsen, L. Hoffmann, M. Budde, R. Jones, J. Goss, and S. Öberg, in *Defects in Semiconductors 18*, edited by M. Suezawa and H. Katayama-Yoshida, Materials Science Forum (Trans-Tech, Aedermannsdorf, Switzerland, 1995), Vols. 196–201, p. 933.

[9] P. Deák, M. Heinrich, L. C. Snyder, and J. W. Corbett, Mater. Sci. Eng. **B4**, 57 (1989).

[10] P. Deák, L. C. Snyder, M. Heinrich, C. R. Ortiz, and J. W. Corbett, Physica B **170**, 253 (1991).

[11] H. J. Stein, J. Electron. Mater. **4**, 159 (1975).

[12] S. J. Pearton, J. W. Corbett, and M. Stavola, *Hydrogen in Crystalline Semiconductors* (Springer-Verlag, Berlin, 1992).

[13] J. D. Holbech, B. Bech Nielsen, R. Jones, P. Sitch, and S. Öberg, Phys. Rev. Lett. **71**, 875 (1993).

[14] M. Budde, B. Bech Nielsen, R. Jones, J. Goss, and S. Öberg, Phys. Rev. B **54**, 5485 (1996).

[15] T. S. Shi, G. R. Bai, M. W. Qi, and J. K. Zhou, Mater. Sci. Forum **10–12**, 597 (1986).

[16] L. M. Xie, M. W. Qi, and J. M. Chen, J. Phys.: Condens. Matter **3**, 8519 (1991).

[17] Y. C. Du, Y. F. Chang, X. T. Meng, and H. Y. Sheng, Sci. Sinica A **30**, 176 (1987).

[18] A. A. Kaplyanskii, Opt. Spectrosk. **16**, 1031 (1964) [Opt. Spectrosc. **16**, 557 (1964)].

[19] A. E. Hughes and W. A. Runciman, Proc. Phys. Soc. London **90**, 827 (1967).

[20] $[h'k'l']$ defines the direction of electrical field vector for the polarized light.

[21] The relative intensities of the split components for [100] and [111] stress are identical for all polarizations perpendicular to the stress direction. For [110] stress, however, the crystal becomes biaxial and the particular direction of polarization perpendicular to the applied stress has to be specified. Normally, two different stress patterns for [110] stress are considered, namely, those with the polarization vector for perpendicular polarization along [001] and [110].

[22] *American Institute of Physics Handbook*, 3rd ed., edited by D. W. E. Gray (McGraw-Hill, New York, 1972), pp. 7–189.

[23] We have the freedom to choose the [001] direction in Fig. 10 so that $0° \leqslant \theta \leqslant 90°$. Moreover, the [100] and [010] direction may be chosen so that $0° \leqslant \varphi \leqslant 90°$. If $\varphi \in [45°, 90°]$, then the equivalent orientation of the defect that is generated by the reflection in the (110) plane would maintain the C_2 axis along [001] and a $\mathbf{n}_1^{\xi}$ vector with the same value of θ, but its azimuthal angle would be in the interval [0°,45°].

[24] Eq. (16) holds whenever the two modes are the symmetric and asymmetric combinations of two equivalent Si-H or Ge-H bonds and, hence, also for orthorhombic-I, orthorhombic-II, and monoclinic-I symmetry if θ is interpreted as half of the angle between $\mathbf{n}_1^{\xi}$ and $\mathbf{n}_2^{\xi}$.

[25] Note that the procedure is not a true second-order perturbation calculation.

[26] R. Jones, Philos. Trans. R. Soc. London, Ser. A **341**, 351 (1992).

[27] J. F. Zheng, M. Stavola, and G. D. Watkins, in *The Physics of Semiconductors*, edited by D. J. Lockwood (World Scientific, Singapore, 1994), p. 2363.

[28] P. Leary, R. Jones, S. Öberg, and V. J. B. Torres, Phys. Rev. B **55**, 2188 (1997).